

Inverting Nonlinear Dimensionality Reduction with Scale-Free Radial Basis Function Interpolation

Nathan D. Monnig^{a,*}, Bengt Fornberg^a, François G. Meyer^b

^aDepartment of Applied Mathematics, UCB 526, University of Colorado at Boulder, Boulder, CO 80309

^bDepartment of Electrical Engineering, UCB 425, University of Colorado at Boulder, Boulder, CO 80309

Abstract

Nonlinear dimensionality reduction embeddings computed from datasets do not provide a mechanism to compute the inverse map. In this paper, we address the problem of computing a stable inverse map to such a general bi-Lipschitz map. Our approach relies on radial basis functions (RBFs) to interpolate the inverse map everywhere on the low-dimensional image of the forward map. We demonstrate that the scale-free cubic RBF kernel performs better than the Gaussian kernel: it does not suffer from ill-conditioning, and does not require the choice of a scale. The proposed construction is shown to be similar to the Nyström extension of the eigenvectors of the symmetric normalized graph Laplacian matrix. Based on this observation, we provide a new interpretation of the Nyström extension with suggestions for improvement.

Keywords: inverse map, nonlinear dimensionality reduction, radial basis function, interpolation, Nyström extension

1. Introduction

The construction of parametrizations of low dimensional data in high dimension is an area of intense research (e.g., [1, 2, 3, 4]). A major limitation of these methods is that they are only defined on a discrete set of data. As a result, the inverse mapping is also only defined on the data. There are well known strategies to extend the forward map to new points—for example, the Nyström extension is a common approach to solve this *out-of-sample extension* problem (see e.g., [5] and references therein). However, the problem of extending the inverse map (i.e. the *preimage problem*) has received little attention so far (but see [6]). The nature of the preimage problem precludes application of the Nyström extension, since it does not involve extension of eigenvectors.

We present a method to numerically invert a general smooth bi-Lipschitz nonlinear dimensionality reduction mapping over all points in the image of the forward map. The method relies on interpolation via radial basis functions of the coordinate functions that parametrize the manifold in high dimension.

The contributions of this paper are twofold. Primarily, this paper addresses a fundamental problem for the analysis of datasets: given the construction of an adaptive parametrization of the data in terms of a small number of coordinates, how does one synthesize new data using new values of the coordinates? We provide a simple and elegant solution to solve the “preimage problem”. Our approach is scale-free and numerically stable and can be applied to any nonlinear dimension reduction technique. The second contribution is a novel interpretation of the Nyström extension as a properly rescaled radial basis function interpolant. A precise analysis of this similarity yields a critique of the Nyström extension, as well as suggestions for improvement.

*Corresponding author

Email address: E-mail: nathan.monnig@colorado.edu (Nathan D. Monnig)

URL: <http://amath.colorado.edu/student/monnig/> (Nathan D. Monnig)

2. The Inverse Mapping

2.1. Definition of the problem, and approach

We consider a finite set of n datapoints $\{\mathbf{x}^{(1)}, \dots, \mathbf{x}^{(n)}\} \subset \mathbb{R}^D$ that lie on a bounded low-dimensional smooth manifold $\mathcal{M} \subset \mathbb{R}^D$, and we assume that a nonlinear mapping has been defined for each point $\mathbf{x}^{(i)}$,

$$\Phi_n : \mathcal{M} \subset \mathbb{R}^D \longrightarrow \mathbb{R}^d \quad (1)$$

$$\mathbf{x}^{(i)} \longmapsto \mathbf{y}^{(i)} = \Phi_n(\mathbf{x}^{(i)}), \quad i = 1, \dots, n. \quad (2)$$

We further assume that the map Φ_n converges toward a limiting continuous function, $\Phi : \mathcal{M} \rightarrow \Phi(\mathcal{M})$, when the number of samples goes to infinity. Such limiting maps exist for algorithms such as the Laplacian eigenmaps [2].

In practice, the construction of the map Φ_n is usually only the first step. Indeed, one is often interested in exploring the configuration space in \mathbb{R}^d , and one needs an inverse map to synthesize a new measurement \mathbf{x} for a new configuration $\mathbf{y} = [y_1 \ \dots \ y_d]^T$ in the coordinate domain (see e.g., [7]). In other words, we would like to define an inverse map $\Phi_n^{-1}(\mathbf{y})$ at any point $\mathbf{y} \in \Phi_n(\mathcal{M})$. Unfortunately, unlike linear methods (such as PCA), nonlinear dimension reduction algorithms only provide an explicit mapping for the original discrete dataset $\{\mathbf{x}^{(1)}, \dots, \mathbf{x}^{(n)}\}$. Therefore, the inverse mapping Φ_n^{-1} is only defined on these data.

The goal of the present work is to generate a numerical extension of Φ_n^{-1} to all of $\Phi(\mathcal{M}) \subset \mathbb{R}^d$. To simplify the problem, we assume the mapping Φ_n coincides with the limiting map Φ on the data, $\Phi_n(\mathbf{x}^{(i)}) = \Phi(\mathbf{x}^{(i)})$ for $i = 1, \dots, n$. This assumption allows us to rephrase the problem as follows: we seek an extension of the map Φ^{-1} everywhere on $\Phi(\mathcal{M})$, given the knowledge that $\Phi^{-1}(\mathbf{y}^{(i)}) = \Phi_n^{-1}(\mathbf{y}^{(i)}) = \mathbf{x}^{(i)}$. We address this problem using interpolation, and we construct an approximate inverse Φ_n^\dagger , which converges toward the true inverse as the number of samples, n , goes to infinity,

$$\Phi^\dagger : \Phi(\mathcal{M}) \rightarrow \mathbb{R}^D, \quad \text{with} \quad \Phi^\dagger(\mathbf{y}^{(i)}) = \mathbf{x}^{(i)}, \quad (3)$$

$$\text{and} \quad \forall \mathbf{y} \in \Phi(\mathcal{M}), \quad \lim_{n \rightarrow \infty} \Phi_n^\dagger(\mathbf{y}) = \Phi^{-1}(\mathbf{y}). \quad (4)$$

Using terminology from geometry, we call $\Phi(\mathcal{M})$ the *coordinate domain*, and Φ^{-1} a *coordinate map* that parametrizes the manifold $\mathcal{M} = \{\mathbf{x} \in \mathbb{R}^D; \mathbf{x} = \Phi^{-1}(\mathbf{y}), \mathbf{y} \in \Phi(\mathcal{M})\}$. The components of $\Phi^{-1} = [\phi_1^{-1} \ \dots \ \phi_D^{-1}]^T$ are the *coordinate functions*. We note that the focus of the paper is not the construction of new points \mathbf{y} in the coordinate domain, but rather the computation of the coordinate functions everywhere in $\Phi(\mathcal{M})$.

2.2. Interpolation of multivariate functions defined on scattered data

Given the knowledge of the inverse at the points $\mathbf{y}^{(i)}$, we wish to interpolate Φ^{-1} over $\Phi(\mathcal{M})$. We propose to interpolate each coordinate function, $\phi_i^{-1}(\mathbf{y})$, $i = 1, \dots, D$ independently of each other. We are thus facing the problem of interpolating a function of several variables defined on the manifold $\Phi(\mathcal{M})$. Most interpolation techniques that are designed for single variable functions can only be extended using tensor products, and have very poor performance in several dimensions. For instance, we know from Mairhuber theorem (e.g., [8]) that we should not use a basis independent of the nodes (for example, polynomial) to interpolate scattered data in dimension $d > 1$. As a result, few options exist for multivariate interpolation. Some of the most successful interpolation methods involve Radial Basis Functions (RBFs) [8]. Therefore, we propose to use RBFs to construct the inverse mapping. Similar methods have been explored in [6, 9] to interpolate data on a low-dimensional manifold. We note that while kriging [10] is another common approach for interpolating scattered data, most kriging techniques are equivalent to RBF interpolants [11]. In fact, because in our application we lack specialized information about the covariance structure of the inverse map, kriging is identical to RBF interpolation.

We focus our attention on two basis functions: the Gaussian and the cubic. These functions are representative of the two main classes of radial functions: scale dependent, and scale invariant. In the experimental section we compare the RBF methods to Shepard's method [12], an approach for multivariate interpolation and approximation that is used extensively in computer graphics [13], and which was recently proposed in [14] to compute a similar inverse map.

For each coordinate function ϕ_i^{-1} , we define ϕ_i^\dagger to be the RBF interpolant to the data $(\mathbf{y}^{(i)}, \mathbf{x}^{(i)})$,

$$\text{for all } \mathbf{y} \in \Phi(\mathcal{M}), \quad \phi_i^\dagger(\mathbf{y}) = \sum_{j=1}^n \alpha_i^{(j)} k(\mathbf{y}, \mathbf{y}^{(j)}). \quad (5)$$

The reader will notice that we dropped the dependency on n (number of samples) in $\Phi^\dagger = [\phi_1^\dagger \dots \phi_D^\dagger]^T$ to ease readability. The function k in (5) is the kernel that defines the radial basis functions, $k(\mathbf{z}, \mathbf{w}) = g(\|\mathbf{z} - \mathbf{w}\|)$. The weights, $\{\alpha_i^{(1)}, \dots, \alpha_i^{(n)}\}$, are determined by imposing the fact that the interpolant be exact at the nodes $\mathbf{y}^{(1)}, \dots, \mathbf{y}^{(n)}$, and thus are given by the solution of the linear system

$$\begin{bmatrix} k(\mathbf{y}^{(1)}, \mathbf{y}^{(1)}) & \dots & k(\mathbf{y}^{(1)}, \mathbf{y}^{(n)}) \\ \vdots & \ddots & \vdots \\ k(\mathbf{y}^{(n)}, \mathbf{y}^{(1)}) & \dots & k(\mathbf{y}^{(n)}, \mathbf{y}^{(n)}) \end{bmatrix} \begin{bmatrix} \alpha_i^{(1)} \\ \vdots \\ \alpha_i^{(n)} \end{bmatrix} = \begin{bmatrix} x_i^{(1)} \\ \vdots \\ x_i^{(n)} \end{bmatrix}. \quad (6)$$

We can combine the D linear systems (6) by concatenating all the coordinates in the right-hand side of (6), and the corresponding unknown weights on the left-hand side of (6) to form the system of equations,

$$\begin{bmatrix} k(\mathbf{y}^{(1)}, \mathbf{y}^{(1)}) & \dots & k(\mathbf{y}^{(1)}, \mathbf{y}^{(n)}) \\ \vdots & \ddots & \vdots \\ k(\mathbf{y}^{(n)}, \mathbf{y}^{(1)}) & \dots & k(\mathbf{y}^{(n)}, \mathbf{y}^{(n)}) \end{bmatrix} \begin{bmatrix} \alpha_1^{(1)} & \alpha_D^{(1)} \\ \vdots & \vdots \\ \alpha_1^{(n)} & \alpha_D^{(n)} \end{bmatrix} = \begin{bmatrix} x_1^{(1)} & x_D^{(1)} \\ \vdots & \vdots \\ x_1^{(n)} & x_D^{(n)} \end{bmatrix}, \quad (7)$$

which takes the form $KA = X$, where $K_{i,j} = k(\mathbf{y}^{(i)}, \mathbf{y}^{(j)})$, $A_{i,j} = \alpha_j^{(i)}$, and $X_{i,j} = x_j^{(i)}$. Let us define the vector $\mathbf{k}(\mathbf{y}, \cdot) = [k(\mathbf{y}, \mathbf{y}^{(1)}) \dots k(\mathbf{y}, \mathbf{y}^{(n)})]^T$. The approximate inverse at a point $\mathbf{y} \in \Phi(\mathcal{M})$ is given by

$$\Phi^\dagger(\mathbf{y})^T = \mathbf{k}(\mathbf{y}, \cdot)^T A = \mathbf{k}(\mathbf{y}, \cdot)^T K^{-1} X. \quad (8)$$

3. Convergence of RBF Interpolants

3.1. Invertibility and Conditioning

The approximate inverse (8) is obtained by interpolating the original data $(\mathbf{y}^{(i)}, \mathbf{x}^{(i)})$ using RBFs. In order to assess the quality of this inverse, three questions must be addressed: 1) Given the set of interpolation nodes, $\{\mathbf{y}^{(i)}\}$, is the interpolation matrix K in (7) necessarily non-singular and well-conditioned? 2) How well does the interpolant (8) approximate the true inverse Φ^{-1} ? 3) What convergence rate can we expect as we populate the domain with additional nodes? In this section we provide elements of answers to these three questions. For a detailed treatment, see [8, 15].

In order to interpolate with a radial basis function $k(\mathbf{z}, \mathbf{w}) = g(\|\mathbf{z} - \mathbf{w}\|)$, the system (7) should have a unique solution and be well-conditioned. In the case of the Gaussian defined by

$$k(\mathbf{z}, \mathbf{w}) = \exp(-\varepsilon^2 \|\mathbf{z} - \mathbf{w}\|^2), \quad (9)$$

the eigenvalues of K in (7) follow patterns in the powers of ε that increase with successive eigenvalues, which leads to rapid ill-conditioning of K with increasing n (e.g., [16]; see also [17] for a discussion of the numerical rank of the Gaussian kernel). The resulting interpolant will exhibit numerical *saturation error*. This issue is common among many scale-dependent RBF interpolants. The Gaussian scale parameter, ε , must be selected to match the spacing of the interpolation nodes. One commonly used measure of node spacing is the *fill distance*, the maximum distance from an interpolation node.

Definition 1. For the domain $\Omega \subset \mathbb{R}^d$ and a set of interpolation nodes $Z = \{\mathbf{z}^{(1)}, \dots, \mathbf{z}^{(n)}\} \subset \Omega$ the fill distance, $h_{Z,\Omega}$, is defined by

$$h_{Z,\Omega} := \sup_{z \in \Omega} \min_{z^{(j)} \in Z} \|z - z^{(j)}\|. \quad (10)$$

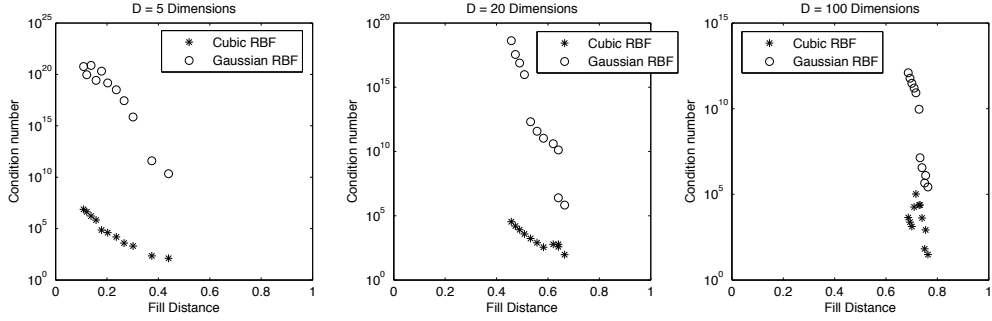


Figure 1: Condition number of K in (7), for the Gaussian (\circ) and the cubic ($*$) as a function of the fill distance for a fixed scale $\varepsilon = 10^{-2}$. Points are randomly scattered on the first quadrant of the unit sphere in \mathbb{R}^D , for $D = 5, 20, 100$ from left to right. Note: the same range of n , from 10 to 1000, was used in each dimension. In high dimension, it takes a large number of points to reduce fill distance. However, the condition number of K still grows rapidly for increasing n .

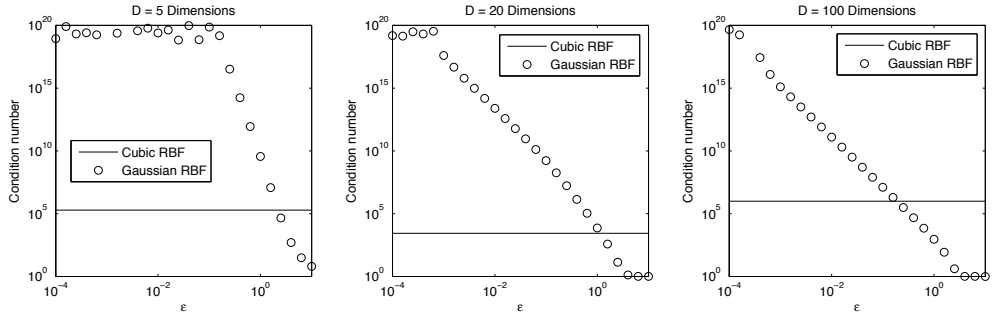


Figure 2: Condition number of K in (7), for the Gaussian (\circ) and the cubic ($-$) as a function of the scale ε , for a fixed fill distance. $n = 200$ points are randomly scattered on the first quadrant of the unit sphere in \mathbb{R}^D , $D = 5, 20, 100$ from left to right.

Owing to the difficulty in precisely establishing the boundary of a domain $\Omega \subset \mathbb{R}^d$ defined by a discrete set of sampled data, estimating the fill distance $h_{Z,\Omega}$ is somewhat difficult in practice. Additionally, the fill distance is a measure of the “worst case”, and may not be representative of the “typical” spacing between nodes. Thus, we consider a proxy for fill distance which depends only on mutual distances between the data points. We define the *local fill distance*, \bar{h}_{local} , to denote the average distance to a nearest neighbor,

$$\bar{h}_{\text{local}} := \frac{1}{n} \sum_{i=1}^n \min_{j \neq i} \|z^{(i)} - z^{(j)}\|. \quad (11)$$

The relationship between the condition number of K and the spacing of interpolation nodes is explored in Fig. 1, where we observe rapid ill-conditioning of K with respect to decreasing local fill distance, \bar{h}_{local} . Conversely, if \bar{h}_{local} remains constant while ε is reduced, the resulting interpolant improves until ill-conditioning of the K matrix leads to propagation of numerical errors, as is shown in Fig. 2. When interpolating with the Gaussian kernel, the choice of the scale parameter ε is difficult. On the one hand, smaller values of ε likely lead to a better interpolant. For example, in 1- d , a Gaussian RBF interpolant will converge to the Lagrange interpolating polynomial in the limit as $\varepsilon \rightarrow 0$ [18]. On the other hand, the interpolation matrix becomes rapidly ill-conditioned for decreasing ε . While some stable algorithms have been recently proposed to generate RBF interpolants (e.g., [19], and references therein)

these sophisticated algorithms are more computationally intensive and algorithmically complex than the RBF-Direct method used in this paper, making them undesirable for the inverse-mapping interpolation task.

Saturation error can be avoided by using the scale-free RBF kernel $g(\|z - \mathbf{w}\|) = \|z - \mathbf{w}\|^3$, one instance from the set of RBF kernels known as the *radial powers*,

$$g(\|z - \mathbf{w}\|) = \|z - \mathbf{w}\|^\rho \quad \text{for } \rho = 1, 3, 5, \dots \quad (12)$$

Together with the *thin plate splines*,

$$g(\|z - \mathbf{w}\|) = \|z - \mathbf{w}\|^\rho \log \|z - \mathbf{w}\| \quad \text{for } \rho = 2, 4, 6, \dots, \quad (13)$$

they form the family of RBFs known as the *polyharmonic splines*.

Because it is a monotonically increasing function, the cubic kernel, $\|z - \mathbf{w}\|^3$, may appear less intuitive than the Gaussian. The importance of the cubic kernel stems from the fact that the space generated by linear combinations of shifted copies of the kernel is composed of splines. In one dimension, one recovers the cubic spline interpolant. One should note that the behavior of the interpolant in the far field (away from the boundaries of the convex hull of the samples) can be made linear (by adding constants and linear polynomials) as a function of the distance, and therefore diverges much more slowly than r^3 [20].

In order to prove the existence and uniqueness of an interpolant of the form,

$$\phi_i^\dagger(\mathbf{y}) = \sum_{j=1}^n \alpha_i^{(j)} \|\mathbf{y} - \mathbf{y}^{(j)}\|^3 + \gamma_i + \sum_{k=1}^d \beta_{k,i} y_k, \quad (14)$$

we require that the set $\{\mathbf{y}^{(1)}, \dots, \mathbf{y}^{(n)}\}$ be a 1-unisolvent set in \mathbb{R}^d , where *m-unisolvency* is as follows.

Definition 2. *The set of nodes $\{\mathbf{z}^{(1)}, \dots, \mathbf{z}^{(n)}\} \subset \mathbb{R}^d$ is called *m-unisolvent* if the unique polynomial of total degree at most *m* interpolating zero data on $\{\mathbf{z}^{(1)}, \dots, \mathbf{z}^{(n)}\}$ is the zero polynomial.*

For our problem, the condition that the set of nodes $\{\mathbf{y}^{(j)}\}$ be 1-unisolvent is equivalent to the condition that the matrix

$$\begin{bmatrix} 1 & \dots & 1 \\ \left[\mathbf{y}^{(1)} \right] & \dots & \left[\mathbf{y}^{(n)} \right] \end{bmatrix} = \begin{bmatrix} 1 & \dots & 1 \\ \phi_1(\mathbf{x}_1) & \dots & \phi_1(\mathbf{x}_n) \\ \vdots & & \vdots \\ \phi_d(\mathbf{x}_1) & \dots & \phi_d(\mathbf{x}_n) \end{bmatrix} \quad (15)$$

have rank $d + 1$ (we assume that $n \geq d + 1$). This condition is easily satisfied. Indeed, the rows $2, \dots, d + 1$ of (15) are formed by the orthogonal eigenvectors of $D^{-1/2} W D^{-1/2}$. Additionally, the first eigenvector, ϕ_0 , has constant sign. As a result, ϕ_1, \dots, ϕ_d are linearly independent of any other vector of constant sign, in particular $\mathbf{1}$. In Figures 1 and 2 we see that the cubic RBF system exhibits much better conditioning than the Gaussian.

3.2. What Functions Can We Reproduce? the Concept of Native Spaces

We now consider the second question: can the interpolant (5) approximate the true inverse Φ^{-1} to arbitrary precision? As we might expect, an RBF interpolant will converge to functions contained in the completion of the space of linear combinations of the kernel, $\mathcal{H}_k(\Omega) = \text{span}\{k(\cdot, \mathbf{z}) : \mathbf{z} \in \Omega\}$. This space is called the *native space*. We note that the completion is defined with respect to the *k*-norm, which is induced by the inner-product given by the reproducing kernel *k* on the pre-Hilbert space $\mathcal{H}_k(\Omega)$ [8].

It turns out that the native space for the Gaussian RBF is a very small space of functions whose Fourier transforms decay faster than a Gaussian [8]. In practice, numerical issues usually prevent convergence of Gaussian RBF interpolants, even within the native space, and therefore we are not concerned with this issue. The native space of the cubic RBF, on the other hand, is an extremely large space. When the dimension, *d*, is odd, the native space of the cubic RBF is the Beppo Levi space on \mathbb{R}^d of order $l = (d + 3)/2$ [15]. We recall the definition of a *Beppo Levi space* of order *l*.

Definition 3. For $l > d/2$, the linear space $BL_l(\mathbb{R}^d) := \{f \in C(\mathbb{R}^d) : D^\alpha f \in L_2(\mathbb{R}^d), \forall |\alpha| = l\}$, equipped with the inner product $\langle f, g \rangle_{BL_l(\mathbb{R}^d)} = \sum_{|\alpha|=l} \frac{l!}{\alpha!} \langle D^\alpha f, D^\alpha g \rangle_{L_2(\mathbb{R}^d)}$, is called the Beppo Levi space on \mathbb{R}^d of order l , where D^α denotes the weak derivative of (multi-index) order $\alpha \in \mathbb{N}^d$ on \mathbb{R}^d .

For even dimension, the Beppo Levi space on \mathbb{R}^d of order $l = (d + 2)/2$ corresponds to the native space of the thin plate spline $g(\|z - \mathbf{w}\|) = \|z - \mathbf{w}\|^2 \log\|z - \mathbf{w}\|$ [15]. Because we assume that the inverse map Φ^{-1} is smooth, we expect that it belongs to any of the Beppo Levi spaces. Despite the fact that we lack a theoretical characterization of the native space for the cubic RBF in even dimension, all of our numerical experiments have demonstrated equal or better performance of the cubic RBF relative to the thin plate spline in all dimensions (see also [21] for similar conclusions). Thus, to promote algorithmic simplicity for practical applications, we have chosen to work solely with the cubic RBF.

3.3. Convergence Rates

The Gaussian RBF interpolant converges (in L^∞ norm) exponentially fast toward functions in the native space, as a function of the decreasing fill distance $h_{Z,\Omega}$ [8]. However, as observed above, rapid ill-conditioning of the interpolation matrix makes such theoretical results irrelevant without resorting to more costly stable algorithms. The cubic interpolant converges at least as fast as $O(h_{Z,\Omega}^{3/2})$ in the respective native space [15]. In practice, we have experienced faster rates of algebraic convergence, as shown in the experimental section.

4. Experiments

We first conduct experiments on a synthetic manifold, and we then provide evidence of the performance of our approach on real data. For all experiments we quantify the performance of the interpolation using a “leave-one-out reconstruction” approach: we compute $\Phi^\dagger(\mathbf{y}^{(j)})$, for $j = 1, \dots, n$, using the remaining $n - 1$ points: $\{\mathbf{y}^{(1)}, \dots, \mathbf{y}^{(j-1)}, \mathbf{y}^{(j+1)}, \dots, \mathbf{y}^{(n)}\}$ and their coordinates in \mathbb{R}^D , $\{\mathbf{x}^{(1)}, \dots, \mathbf{x}^{(j-1)}, \mathbf{x}^{(j+1)}, \dots, \mathbf{x}^{(n)}\}$. The average performance is then measured using the average leave-one-out L^2 reconstruction error,

$$E_{\text{avg}} = \frac{1}{n} \sum_{j=1}^n \|\mathbf{x}^{(j)} - \Phi^\dagger(\mathbf{y}^{(j)})\|. \quad (16)$$

In order to quantify the effect of the sampling density on the reconstruction error, we compute E_{avg} as a function of \bar{h}_{local} , which is defined by (11). The two RBF interpolants are compared to Shepard’s method, a multivariate interpolation/approximation method used extensively in computer graphics [13]. Shepard’s method computes the optimal constant function that minimizes the sum of squared errors within a neighborhood \mathcal{N}_y of \mathbf{y} in \mathbb{R}^d , weighted according to their proximity to \mathbf{y} . The solution to this moving least squares approximation is given by

$$\Phi_{\text{Shepard}}^\dagger(\mathbf{y}) = \sum_{j: \mathbf{y}^{(j)} \in \mathcal{N}_y} \frac{\exp(-\varepsilon^2 \|\mathbf{y} - \mathbf{y}^{(j)}\|^2)}{\sum_{i: \mathbf{y}^{(i)} \in \mathcal{N}_y} \exp(-\varepsilon^2 \|\mathbf{y} - \mathbf{y}^{(i)}\|^2)} \mathbf{x}^{(j)}. \quad (17)$$

The relative impact of neighboring function values is controlled by the scale parameter ε , which we choose to be a multiple of $1/\bar{h}_{\text{local}}$.

4.1. Unit Sphere in \mathbb{R}^D

For our synthetic manifold example, we sampled n points $\{\mathbf{x}^{(1)}, \dots, \mathbf{x}^{(n)}\}$ from the uniform distribution on the unit sphere S^4 , then embedded these data in \mathbb{R}^{10} via a random unitary transformation. The data are mapped to $\{\mathbf{y}^{(1)}, \dots, \mathbf{y}^{(n)}\} \subset \mathbb{R}^d = \mathbb{R}^5$ using the first five non-trivial eigenvectors of the graph Laplacian. The minimum of the total number of available neighbors, $n - 1$, and 200 neighbors was used to compute the interpolant. For each local fill distance, \bar{h}_{local} , the average reconstruction error is computed using (16). The performances of the cubic RBF, Gaussian RBF, and Shepard’s method versus \bar{h}_{local} are shown in Fig. 3. We note that the interpolation error based on the cubic RBF is lowest, and appears to scale approximately with $O(\bar{h}_{\text{local}}^{-2})$, an improvement over the $O(h_{Z,\Omega}^{3/2})$ bound [15]. In fact, the cubic RBF proves to be extremely accurate, even with a very sparsely populated domain: the largest \bar{h}_{local} corresponds to 10 points scattered on S^4 .

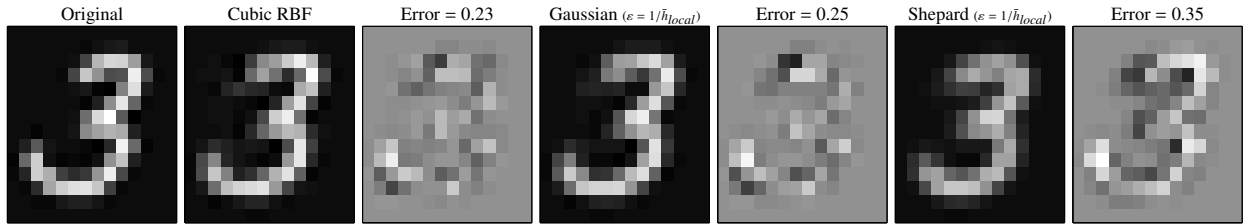


Figure 4: From left to right: original image to be reconstructed; reconstructions using the different methods, each followed by the residual error: cubic RBF, Gaussian RBF, and Shepard’s method.

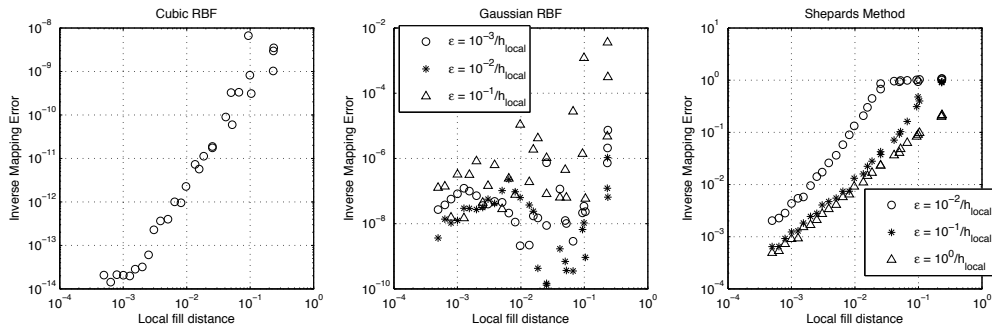


Figure 3: Average leave-one-out reconstruction residual, E_{avg} , on S^4 embedded in \mathbb{R}^{10} , using the cubic (left), the Gaussian (center), and Shepard’s method (right). Note the difference in the range of y-axis.

	scale ($\varepsilon \times \bar{h}_{\text{local}}$)	0	1	2	3	4	5	6	7	8	9
Cubic	—	0.248	0.135	0.349	0.334	0.299	0.350	0.259	0.261	0.354	0.262
	0.5	0.319	0.169	0.421	0.417	0.362	0.424	0.315	0.314	0.452	0.313
Gaussian	1	0.305	0.223	0.375	0.363	0.345	0.382	0.310	0.322	0.369	0.312
	2	0.457	0.420	0.535	0.505	0.513	0.554	0.477	0.497	0.491	0.478
Shepard	0.5	0.422	0.271	0.511	0.489	0.475	0.508	0.439	0.453	0.474	0.434
	1	0.302	0.175	0.396	0.385	0.348	0.378	0.314	0.318	0.379	0.309
	2	0.303	0.186	0.400	0.382	0.362	0.402	0.320	0.325	0.382	0.320

Table 1: Reconstruction error E_{avg} for each digit (0-9). Red denotes lowest average reconstruction residual.

4.2. Handwritten Digits Datasets

In addition to the previous synthetic example, the performance of the inverse mapping algorithm was also assessed on a “naturally occurring” high-dimensional data set: a set of digital images of handwritten digits. The data set (obtained from the MNIST database [22]) consists of 1,000 handwritten images of the digits 0 to 9. The images were originally centered and normalized to have size 28×28 . In our experiments, the images were further resized to 14×14 pixels and normalized to have unit l^2 norm. We obtained 10 different datasets, each consisting of 1,000 points in \mathbb{R}^{196} . The dimension reduction and subsequent leave-one-out reconstruction were conducted on the dataset corresponding to a specific digit, independently of the other digits. For each digit, a 10-dimensional representation of the 1,000 images was generated using Laplacian Eigenmaps [2]. Then the inverse mapping techniques were evaluated on all images in the set. Table 1 shows the reconstruction error E_{avg} for the three methods, for all digits. Fig. 4 shows

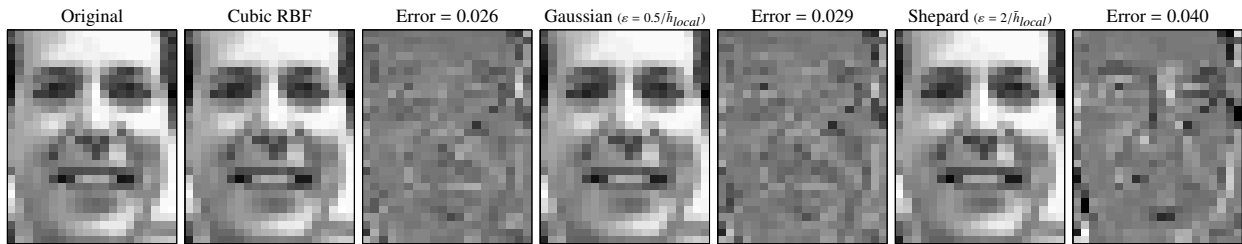


Figure 5: From left to right: original image to be reconstructed; reconstructions using the different methods, each followed by the residual error: cubic RBF, Gaussian RBF, and Shepard’s method.

	Cubic	Gaussian			Shepard		
Scale ($\epsilon \times \bar{h}_{\text{local}}$)	—	0.25	0.5	1	1	2	4
E_{avg}	0.0361	0.0457	0.0414	0.0684	0.0633	0.0603	0.0672

Table 2: Reconstruction error E_{avg} for the Frey Face dataset. Red denotes lowest average reconstruction residual.

three representative reconstructions for the digit “3”. The optimal scales (according to Table 1) were chosen for both the Gaussian RBF and Shepard’s methods. The cubic RBF outperforms the Gaussian RBF and Shepard’s method in all cases, with the lowest average error (Table 1), and with the most “noise-like” reconstruction residual (Fig. 4). Results suggest that a poor choice of scale parameter with the Gaussian can corrupt the reconstruction. The scale parameter in Shepard’s method must be carefully selected to avoid the two extremes of either reconstructing solely from a single nearest neighbor, or reconstructing a blurry, equally weighted, average of all neighbors.

4.3. Frey Face Dataset

Finally, the performance of the inverse mapping algorithms was also assessed on the Frey Face dataset [23], which consists of digital images of Brendan Frey’s face taken from sequential frames of a short video. The dataset is composed of 20×28 gray scale images. Each image was normalized to have unit l^2 norm, providing a dataset of 1,965 points in \mathbb{R}^{560} . A 15-dimensional representation of the Frey Face dataset was generated via Laplacian eigenmaps. The inverse mapping techniques were tested on all images in the set. Table 2 shows the mean leave-one-out reconstruction errors for the three methods. Fig. 5 shows three representative reconstructions using the different techniques. The optimal scales (according to Table 2) were chosen for both the Gaussian RBF and Shepard’s methods. Again, the cubic RBF outperforms the Gaussian RBF and Shepard’s method in all cases, with the lowest average error (Table 2), and with the most “noise-like” reconstruction residual (Fig. 5).

5. Revisiting Nyström

Inspired by the RBF interpolation method, we provide in the following a novel interpretation of the Nyström extension: the Nyström extension interpolates the eigenvectors of the (symmetric) normalized Laplacian matrix using a slightly modified RBF interpolation scheme. While several authors have mentioned the apparent similarity of Nyström method to RBF interpolation, the novel and detailed analysis provided below provides a completely new insight into the limitations and potential pitfalls of the Nyström extension.

Consistent with Laplacian eigenmaps, we consider the symmetric normalized kernel $\tilde{K} = D^{-1/2}KD^{-1/2}$, where $K_{ij} = k(\mathbf{x}^{(i)}, \mathbf{x}^{(j)})$ is a radial function measuring the similarity between $\mathbf{x}^{(i)}$ and $\mathbf{x}^{(j)}$, and D is the degree matrix (diagonal matrix consisting of the row sums of K).

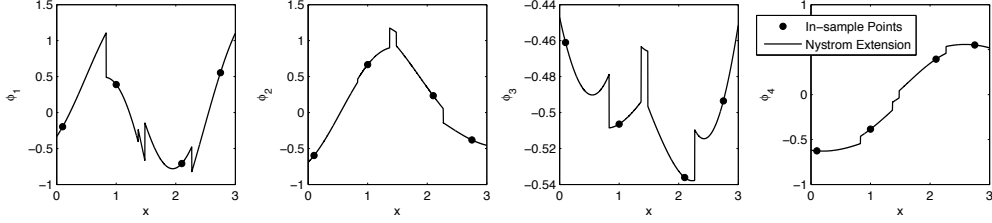


Figure 6: Example of Nyström extension of the eigenvectors of a thresholded Gaussian affinities matrix.

Given an eigenvector ϕ_l of \tilde{K} (associated with a nontrivial eigenvalue λ_l) defined over the points $\mathbf{x}^{(j)}$, the Nyström extension of ϕ_l to an arbitrary new point \mathbf{x} is given by the interpolant

$$\phi_l(\mathbf{x}) = \frac{1}{\lambda_l} \sum_{j=1}^n \tilde{k}(\mathbf{x}, \mathbf{x}^{(j)}) \phi_l(\mathbf{x}^{(j)}), \quad (18)$$

where $\phi_l(\mathbf{x}^{(j)})$ is the coordinate j of the eigenvector $\phi_l = [\phi_l(\mathbf{x}^{(1)}) \ \dots \ \phi_l(\mathbf{x}^{(n)})]^T$. We now proceed by re-writing $\phi_l(\mathbf{x})$ in (18), using the notation $\tilde{\mathbf{k}}(\mathbf{x}, \cdot) = [\tilde{k}(\mathbf{x}, \mathbf{x}^{(1)}) \ \dots \ \tilde{k}(\mathbf{x}, \mathbf{x}^{(n)})]^T$, where $\tilde{k}(\mathbf{x}, \mathbf{x}^{(j)}) = k(\mathbf{x}, \mathbf{x}^{(j)}) / \sqrt{d(\mathbf{x})d(\mathbf{x}^{(j)})}$, and $d(\mathbf{x}) = \sum_{i=1}^n k(\mathbf{x}, \mathbf{x}^{(i)})$.

$$\begin{aligned} \phi_l(\mathbf{x}) &= \lambda_l^{-1} \tilde{\mathbf{k}}(\mathbf{x}, \cdot)^T \phi_l = \tilde{\mathbf{k}}(\mathbf{x}, \cdot)^T \Phi \Lambda^{-1} [0 \ \dots \ 1 \ \dots \ 0]^T = \tilde{\mathbf{k}}(\mathbf{x}, \cdot)^T \Phi \Lambda^{-1} \Phi^T \phi_l \\ &= \tilde{\mathbf{k}}(\mathbf{x}, \cdot)^T \tilde{K}^{-1} \phi_l = \frac{1}{\sqrt{d(\mathbf{x})}} [k(\mathbf{x}, \mathbf{x}^{(1)}) \ \dots \ k(\mathbf{x}, \mathbf{x}^{(n)})] D^{-1/2} (D^{1/2} K^{-1} D^{1/2}) \phi_l \\ &= \frac{1}{\sqrt{d(\mathbf{x})}} \mathbf{k}(\mathbf{x}, \cdot)^T K^{-1} (D^{1/2} \phi_l). \end{aligned} \quad (19)$$

If we compare the last line of (19) to (8), we conclude that in the case of Laplacian Eigenmaps, with a nonsingular kernel similarity matrix K , the Nyström extension is computed using a radial basis function interpolation of ϕ_l after a pre-rescaling of ϕ_l by $D^{1/2}$, and post-rescaling by $1/\sqrt{d(\mathbf{x})}$. Although the entire procedure it is not exactly an RBF interpolant, it is very similar and this interpretation provides new insight into some potential pitfalls of the Nyström method.

The first important observation concerns the sensitivity of the interpolation to the scale parameter in the kernel k . As we have explained in section 3.1, the choice of the optimal scale parameter ε for the Gaussian RBF is quite difficult. In fact, this issue has recently received a lot of attention (e.g. [17, 5]). The second observation involves the dangers of sparsifying the similarity matrix. In many nonlinear dimensionality reduction applications, it is typical to sparsify the kernel matrix K by either thresholding the matrix, or keeping only the entries associated with the nearest neighbors of each \mathbf{x}_j . If the Nyström extension is applied to a thresholded Gaussian kernel matrix, then the components of $\mathbf{k}(\mathbf{x}, \cdot)$ as well as $\sqrt{d(\mathbf{x})}$ are discontinuous functions of \mathbf{x} . As a result, $\phi_l(\mathbf{x})$, the Nyström extension of the eigenvector ϕ_l will also be a discontinuous function of \mathbf{x} , as demonstrated in Fig. 6. In the nearest neighbor approach, the extension of the kernel function \tilde{k} to a new point \mathbf{x} is highly unstable and poorly defined. Given this larger issue, the Nyström extension should not be used in this case. In order to interpolate eigenvectors of a sparse similarity matrix, a better interpolation scheme such as a true (non-truncated) Gaussian RBF, or a cubic RBF interpolant could provide a better alternative to Nyström. A local implementation of the interpolation algorithm may provide significant computational savings in certain scenarios.

Acknowledgments

The authors would like to thank the three anonymous reviewers for their excellent comments. NDM was supported by NSF grant DMS 0941476; BF was supported by NSF grant DMS 0914647; FGM was partially supported by NSF grant DMS 0941476, and DOE award DE-SC0004096.

References

- [1] M. Belkin, P. Niyogi, Laplacian eigenmaps for dimensionality reduction and data representation, *Neural Computation* 15 (2003) 1373–1396.
- [2] R.R. Coifman, S. Lafon, Diffusion maps, *Appl. Comput. Harmon. Anal.* 21 (2006) 5–30.
- [3] S.T. Roweis, L.K. Saul, Nonlinear dimensionality reduction by locally linear embedding, *Science* 290 (2000) 2323–2326.
- [4] B. Scholkopf, A. Smola, K.-R. Müller, Kernel principal component analysis, in: *Advances in Kernel Methods—Support Vector Learning*, MIT Press, 1999, pp. 327–352.
- [5] R.R. Coifman, S. Lafon, Geometric harmonics: A novel tool for multiscale out-of-sample extension of empirical functions, *Applied and Computational Harmonic Analysis* 21 (2006) 31–52.
- [6] A. Elgammal, C.-S. Lee, The role of manifold learning in human motion analysis, in: *Human Motion*, Springer, 2008, pp. 25–56.
- [7] R.R. Coifman, I.G. Kevrekidis, S. Lafon, M. Maggioni, B. Nadler, Diffusion maps, reduction coordinates, and low dimensional representation of stochastic systems, *Multiscale Model. Sim.* 7 (2008) 842–864.
- [8] G.E. Fasshauer, *Meshfree Approximation Methods With MATLAB*, Interdisciplinary Mathematical Sciences, World Scientific, 2007.
- [9] M. J. D. Powell, Radial basis function methods for interpolation to functions of many variables, in: *HERCMA*, 2001, pp. 2–24.
- [10] H. Wackernagel, *Multivariate Geostatistics. An Introduction with Applications*, Springer, 1998.
- [11] M. Scheuerer, R. Schaback, M. Schlather, Interpolation of spatial data – a stochastic or a deterministic problem?, *European Journal of Applied Mathematics* 24 (2013) 601–629.
- [12] D. Shepard, A two-dimensional interpolation function for irregularly-spaced data, in: *Proceedings of the 1968 23rd ACM national conference*, ACM, New York, NY, USA, 1968, pp. 517–524.
- [13] J.P. Lewis, F. Pighin, K. Anjyo, Scattered data interpolation and approximation for computer graphics, in: *ACM SIGGRAPH ASIA 2010 Courses*, ACM, New York, NY, USA, 2010, pp. 2:1–2:73.
- [14] D. Kushnir, A. Haddad, R.R. Coifman, Anisotropic diffusion on sub-manifolds with application to earth structure classification, *Applied and Computational Harmonic Analysis* 32 (2012) 280–294.
- [15] H. Wendland, *Scattered Data Approximation*, Cambridge Monographs on Applied and Computational Mathematics, Cambridge University Press, 2004.
- [16] B. Fornberg, J. Zuev, The Runge phenomenon and spatially variable shape parameters in RBF interpolation, *Comput. Math. Appl.* 54 (2007) 379–398.
- [17] A. Bermanis, A. Averbuch, R.R. Coifman, Multiscale data sampling and function extension, *Applied and Computational Harmonic Analysis* 34 (2013) 15–29.
- [18] T.A. Driscoll, B. Fornberg, Interpolation in the limit of increasingly flat radial basis functions, *Comput. Math. Appl.* 43 (2002) 413–422.
- [19] B. Fornberg, E. Lehto, C. Powell, Stable calculation of Gaussian-based RBF-FD stencils, *Comput. Math. Appl.* 65 (2013) 627–637.
- [20] B. Fornberg, T.A. Driscoll, G. Wright, R. Charles, Observations on the behavior of radial basis function approximations near boundaries, *Comput. Math. Appl.* 43 (2002) 473–490.
- [21] S.M. Wild, C.A. Shoemaker, Global convergence of radial basis function trust region derivative-free algorithms, *SIAM Journal on Optimization* 21 (2011) 761–781.
- [22] S. Gangaputra, Handwritten digit database, <http://cis.jhu.edu/~sachin/digit/digit.html>, 2012.
- [23] S. Roweis, Frey face dataset, <http://cs.nyu.edu/~roweis/data.html>, 2013.